Received: 4 December 2021 | Revised: 9 August 2022 | Accepted: 30 August 2022

DOI: 10.1002/nag.3450

RESEARCH ARTICLE

WILEY

# Application of a coupled hydro-mechanical interface model in simulating uplifting problems

**Maozhu Peng**[1] | **Yinghui Tian**[2] | **Christophe Gaudin**[1] | **Lihai Zhang**[2] | **Daichao Sheng**[3]

[1]Centre for Offshore Foundation Systems and Ocean Graduate School, The University of Western Australia, Crawley, Perth, Australia

[2]Department of Infrastructure Engineering, The University of Melbourne, Parkville, Victoria, Australia

[3]School of Civil & Environmental Engineering, University of Technology Sydney, Broadway, New South Wales, Australia

**Correspondence**
Yinghui Tian, Department of Infrastructure Engineering, The University of Melbourne, Parkville, VIC 3010, Australia.
Email: yinghui.tian@unimelb.edu.au

**Abstract**

This paper presents the detailed formulation of a coupled hydro-mechanical structure-soil interface and demonstrates its application in simulating uplifting problems. This interface features real-time prediction of the pore pressure generation and structure-soil separation, and thus rate dependency and 'breakaway' can be modeled without user intervention. Constitutive relations of this interface were derived by considering the coupling between soil skeleton and fluid along the interface. A complete finite element formulation and numerical implementation of the interface is provided based on an eight-node element. The performance of this interface is demonstrated by simulating lifting a surface footing at varying rates (spanning across undrained, partially drained and drained conditions), compared with existing theoretical solutions, numerical results and experimental data. The good agreement achieved indicates that this interface is capable of modelling uplift at varying rates, which is an extremely challenging topic in offshore engineering. Sensitivity studies were conducted to investigate the parameters affecting uplifting behaviour. A unified backbone curve was established correspondingly, which is shown to be different from existing studies in compression, due to the difference in the mechanism between the two cases.

**KEYWORDS**

breakaway, hydro-mechanical coupled interface, rate dependency, soil-structure interaction, uplifting

## 1 | INTRODUCTION

Modelling structure-soil interaction is a key aspect of numerical analyses of geotechnical problems. Most early interface models[1–6] are mechanically formulated within a total stress framework. But in most cases, soils are filled with pore water, and the structure-soil interaction is closely related to the drainage condition in soil and at the interface. Thus,

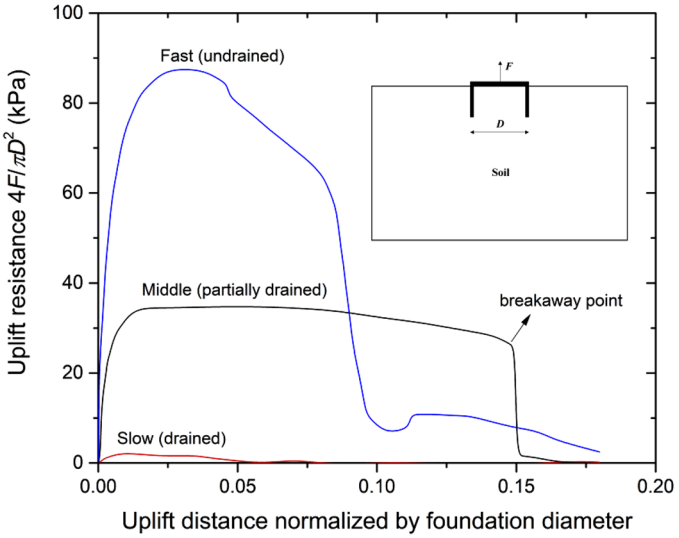


**FIGURE 1** Schematic illustration of drainage dependency of uplift capacity

purely mechanical interfaces are inadequate, and coupled hydro-mechanical interfaces are needed to describe the coupled behaviour of soil skeleton and pore water.

Such an interface is especially needed to model offshore structures subjected to uplift (such as embedded anchors and shallow foundations), because the negative pore pressure (suction) generated at the structure underside plays a key role during the uplift.[7–9] Li[10] conducted a series of centrifuge tests lifting a skirted foundation at varying rates, and the results (Figure 1) indicated two distinct features: (1) the peak resistance increases with uplift rate; and (2) there is a 'breakaway' occurring, where the resistance drops almost to zero in a short time. The two features are closely related to the pore pressure generation/dissipation and the structure-soil separation at the foundation underside, and a hydro-mechanical coupled interface is necessary in order to model this process.

There exists two ways to develop such a coupled hydro-mechanical interface. One is the so-called 'thin layer element' approach, which simulates the interface as a continuum,[5] for example Mana et al.[11] fine-tuned a layer of porous elastic material at the underside of a skirted foundation to represent the interface. This method models seepage appropriately, although the uplift capacity might be overestimated in some instance because of the mechanical strength inevitably introduced by the interface material.

The other method is to model the interface as a 'gap' filled with water,[12–16] which is usually called zero-thickness interface. It opens/closes with water flowing into/draining out of the interface. The effective mechanical stresses become zero when the interface is open while suction can still be sustained, thus allowing a realistic modelling of the separation between the soil skeleton and the structure.

Most of currently available zero-thickness interfaces[12–16] (1) commonly use 4-node or 6-node element (Figure 2) to formulate the interface, with linear interpolations adopted for both displacements and pore pressure; and (2) quantify the water flow along the interface by the cubic law. These are appropriate for most applications. Some specific cases may require quadratic rather than linear interpolations to be used.[17] In addition, the cubic law is mainly applicable for surface structures, and it can overestimate the flow rate for embedded structures, where Darcy's law is believed to be more appropriate as will be discussed later.

This paper presents a coupled hydro-mechanical zero thickness interface by addressing aforementioned issues. The hydraulic behaviours of the interface are divided into transverse flow and longitudinal flow (as shown in Figure 3). The transverse flow adopts the first-order leak-off model proposed by Gerke and van Genuchten.[18] As for longitudinal flow, both cubic flow and Darcy-like flow are considered. The effective mechanical behaviours of the interface are described with linear elasticity along the normal direction and Coulomb friction along the tangential direction. The hydraulic and mechanical aspects are coupled through the principle of mass conservation of the fluid inside the interface. Three mechanical parameters and three hydraulic parameters are required by this interface.

A complete finite element (FE) formulation and numerical implementation are detailed, followed by the simulation of the uplift of a surface footing resting on an elastoplastic seabed at varying rates. To demonstrate its capability, numerical results were compared with experimental observations. Sensitivity studies were then conducted to show the effect of the interface parameters on the uplift behaviour. The results show that the controlling mechanism in uplift is different from

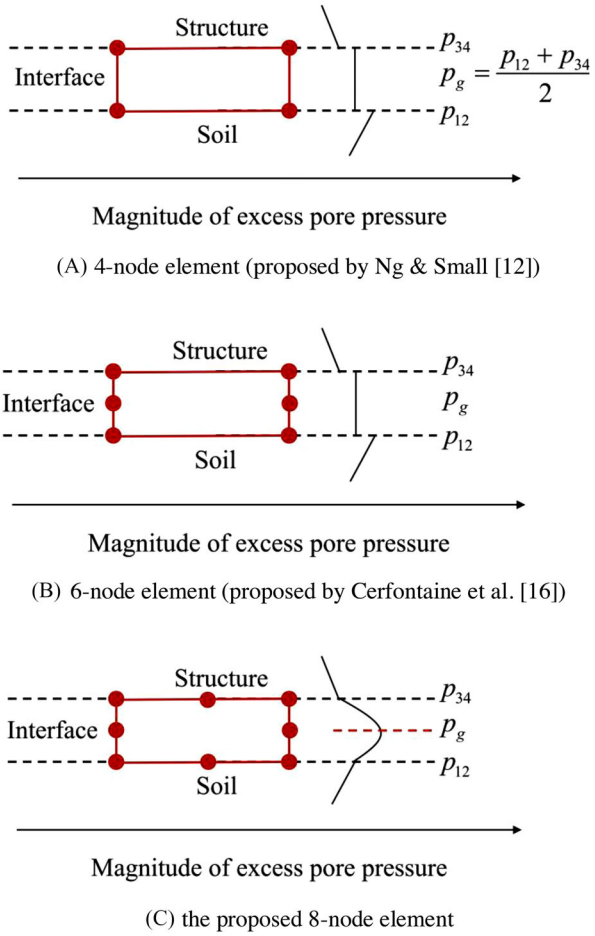


**FIGURE 2** Different types of zero thickness interface element. (A) Four-node element (proposed by Ng & Small[12]). (B) Six-node element (proposed by Cerfontaine et al.[16]). (C) The proposed eight-node element

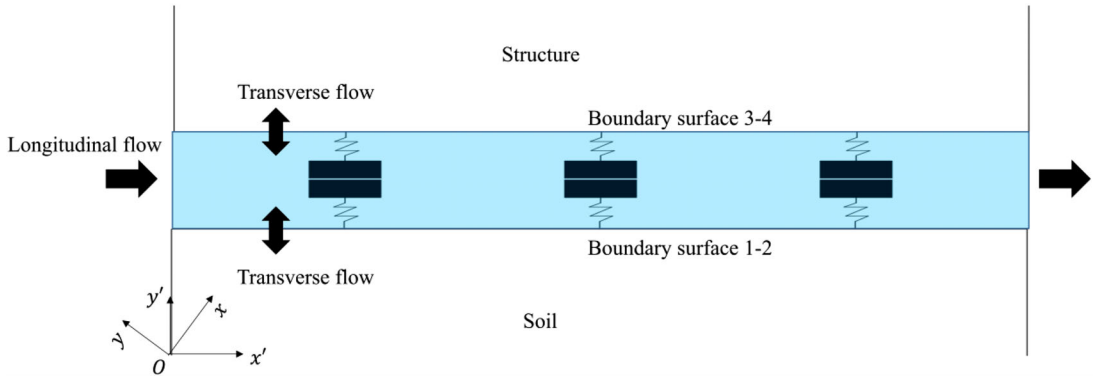


**FIGURE 3** Schematic illustration of the proposed interface

that in compression. A dimensionless velocity is then proposed to normalise uplift rate, and a unified backbone curve is established correspondingly.

## 2 | BEHAVIOURS OF THE INTERFACE AND GOVERNING EQUATIONS

Figure 3 illustrates the proposed interface model, bounded by the soil and the structure with boundary surfaces 1–2 and 3–4. When the structure tends to separate from the soil, the distance between the boundary surfaces 1–2 and 3–4 is to

increase. Thus, suction is generated, drawing water into the interface. When the interface opening width is over a predefined threshold, the effective normal stress reaches zero (i.e. mechanically separated). It is noted that this interface can also be used for compression problems, although this paper focuses on the uplifting cases.

## 2.1 | Boundary conditions

The mechanical boundary conditions of the interface consist of stress boundary ($\mathbf{S_T}$) and displacement boundary ($\mathbf{S_D}$), while the hydraulic boundary conditions comprise of pore pressure boundary ($\mathbf{S_P}$) and fluid velocity boundary ($\mathbf{S_V}$). Their mathematical descriptions are:

$$\begin{aligned} \boldsymbol{\sigma}\mathbf{n} &= \mathbf{T} \quad \text{on } \mathbf{S_T} \\ \mathbf{u} &= \bar{\mathbf{u}} \quad \text{on } \mathbf{S_D} \\ p &= \bar{p} \quad \text{on } \mathbf{S_P} \\ \mathbf{v}\mathbf{n} &= \bar{\mathbf{v}} \quad \text{on} \mathbf{S_V} \end{aligned} \tag{1}$$

where $\boldsymbol{\sigma}$ is the stress tensor on $\mathbf{S_T}$, and $\mathbf{n}$ the outward norm vector of $\mathbf{S_T}$; $\mathbf{T}$ the total stress tensor between the interface and the soil/structure on $\mathbf{S_T}$; $\mathbf{u}$ and $\bar{\mathbf{u}}$ the displacement vector and prescribed displacement vector on $\mathbf{S_D}$; $p$ and $\bar{p}$ the pore pressure and prescribed pore pressure on $\mathbf{S_P}$; $\mathbf{v}$ and $\bar{\mathbf{v}}$ the fluid velocity vector and prescribed fluid velocity vector on $\mathbf{S_V}$. $\bar{\mathbf{u}} = \mathbf{0}$, $\bar{p} = 0$ and $\bar{\mathbf{v}} = \mathbf{0}$ represent displacement-fixed boundary, free drainage boundary and impermeable boundary, respectively.

## 2.2 | Pore pressure distribution

A transversely parabolic distribution of pore pressure is adopted. As in Figure 2(C), $p_{12}$ and $p_{34}$ denote the pore pressures at the boundaries 1–2 and 3–4, respectively, and $p_g$ the pore pressure at the middle of the interface, the pore pressure within a same transverse plane can be expressed as:

$$p = \frac{2\left(p_{12} + p_{34} - 2p_g\right)}{g_n^2} r^2 + \frac{p_{34} - p_{12}}{g_n} r + p_g \tag{2}$$

where $-g_n/2 \leq r \leq g_n/2$ is the vertical distance to the mid-interface (upper part as positive), and $g_n$ the interface opening width.

Hence, the average pore pressure within a transverse plane can be defined as:

$$\bar{p} = \frac{1}{g_n} \int_{-\frac{g_n}{2}}^{\frac{g_n}{2}} p d\,|r| = \frac{1}{6}\left(p_{12} + p_{34} + 4p_g\right) \tag{3}$$

where '| |' means absolute value.

## 2.3 | Transverse flow

The transverse flow accounts for the fluid exchange through the two boundaries (faces 1–2 and 3–4 in Figure 3). This is different from seepage inside soil,[19] and thus Darcy's law is no longer appropriate. In contrast, the first order leak-off model[18] was adopted in this paper:

$$\begin{aligned} v_{12} &= c_{12}\left(\bar{p} - p_{12}\right) = \frac{a_{w1} k_{g1}}{\mu}\left(\bar{p} - p_{12}\right) \\ v_{34} &= c_{34}\left(\bar{p} - p_{34}\right) = \frac{a_{w2} k_{g2}}{\mu}\left(\bar{p} - p_{34}\right) \end{aligned} \tag{4}$$

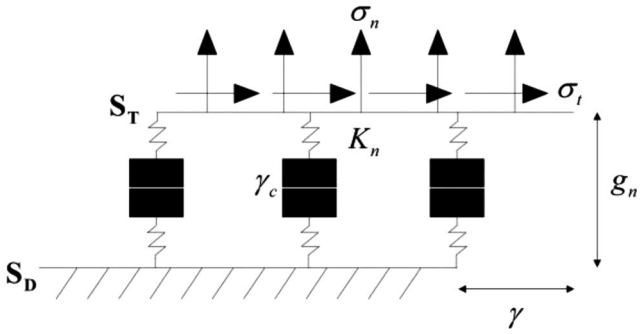


**FIGURE 4** Mechanical response of the interface

where $v_{12}$ and $v_{34}$ are the fluid flow rates at boundaries 1–2 and 3–4, respectively. $c_{12}$ and $c_{34}$ are termed as hydraulic conductivity,[18] which will be discussed later. $a_{w1}$ and $a_{w2}$ (in the unit of $m^{-1}$) are the so-called first-order transfer coefficients for soil and structure, respectively, related to the fluid density and the microstructure of the solid matrix; $k_{g1}$ and $k_{g2}$ ($m^2$) the intrinsic permeability of boundaries 1–2 and 3–4; and μ (Pa•m) the viscosity of fluid.

## 2.4 | Longitudinal flow

The longitudinal flow describes the fluid flow along the interface. For a surface footing on a seabed, the longitudinal flux comes from the ambient free water around the footing and its flow is rarely obstructed by the soil, thus the Navier-Stokes (NS) equations are suitable. For a structure such as a plate anchor deeply buried in soil, the longitudinal flux comes solely from the soil and the flow rate thus depends on soil permeability. Therefore, the flow is Darcy-like, and Darcy's law is more appropriate.

Darcy-like flow considers the longitudinal flow velocity proportional to the longitudinal pore pressure gradient:

$$q_x = g_n \bar{v}_x = \int_{-\frac{g_n}{2}}^{\frac{g_n}{2}} \frac{K_x}{\gamma_w} \frac{\partial p}{\partial x'} d|r| = g_n \frac{K_x}{\gamma_w} \frac{\partial \bar{p}}{\partial x'} \tag{5}$$

where $v_x$ is the longitudinal velocity of Darcy-like flow; $q_x$ the longitudinal flux; and *Ox'* denotes the longitudinal direction of the interface.; $\gamma_w$ the unit weight of water; $K_x$ (m/s) the longitudinal conductivity; its value depends on the properties on surrounding soil, and it is related to the longitudinal permeability $k_x$ ($m^2$) by $K_x = k_x \gamma_w / \mu$. For Darcy-like flow, the longitudinal conductivity $K_x$ is directly treated as a material constant. The value of $g_n K_x$ is usually called interface transmissivity in previous literatures.[16]

The NS equations represent the conservation of linear momentums and mass of the fluid. For simplicity, it is assumed here that the longitudinal flow does not have the acceleration terms. Hence, the NS equations reduce to the static force balance equation of the fluid. As deduced in Appendix 1, the longitudinal flux of NS flow is:

$$q_x = \frac{g_n^3}{120\mu} \left( \frac{dp_{12}}{dx'} + \frac{dp_{34}}{dx'} + 8\frac{dp_g}{dx'} \right) \tag{6}$$

It is worth noting that if transversely uniform pore pressure distribution within the interface is assumed, i.e., $dp_{12}/dx' = dp_{34}/dx' = dp_g/dx'$, Equation (6) becomes $q_x = g_n{}^3 dp_g / 12\mu dx'$. This is the cubic law that has been widely employed in geotechnical problems.[20–25]

## 2.5 | Mechanical behaviours

Figure 4 illustrates the interface subjected to a tension **T** and a displacement boundary $\bar{\mathbf{u}}$. The tension **T** can be decomposed into a normal stress $\sigma_n$ and a shear stress $\sigma_t$ (note this study only considers 2 dimensional problems) which are balanced

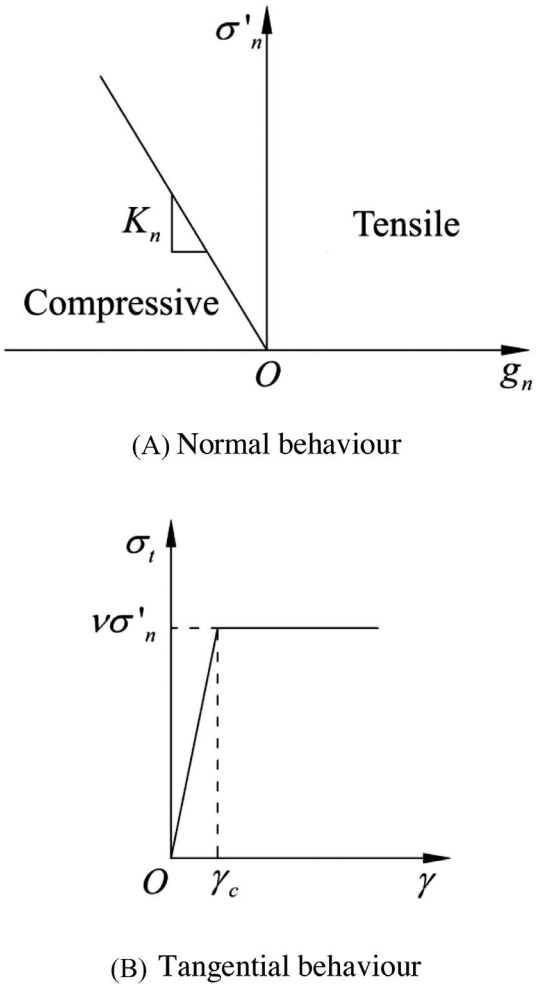


**FIGURE 5** Effective stress-displacement relationship of the interface. (A) Normal behaviour. (B) Tangential behaviour

by the internal effective stresses $\sigma'_n$, $\sigma'_t$ and average pore pressure $\bar{p}$. The force balance equations read:

$$\begin{aligned} \sigma'_n &= \sigma_n - \bar{p} \\ \sigma'_t &= \sigma_t \end{aligned} \tag{7}$$

where positive $\sigma'_n$ means tension, and positive $\sigma'_t$ means the interface deforms in an anti-clockwise way under shearing.

The internal effective stresses $\sigma'_n$ and $\sigma'_t$ control the mechanical behaviours of the interface. The change in interface thickness $\Delta g_n$ is proportionally related to the increment of effective normal stress $\Delta\sigma'_n$ through the normal stiffness $K_n$. The magnitude of $K_n$ is negligible when $g_n$ is beyond a threshold, while its value is large enough to avoid over-penetration when $g_n$ is below this threshold. The tangential behaviour obeys Coulomb friction theory, where the interface first undergoes an elastic shear displacement up to a critical slip distance $\gamma_c$. Beyond $\gamma_c$, plastic shearing (sliding) ensues, and the effective shear stress $\sigma'_t$ reaches a stabilised value $\nu\sigma'_n$, where $\nu$ is the coefficient of friction of the interface. The magnitude of $\gamma_c$ is likely to be dependent on $\sigma'_n$. But acknowledging that $\gamma_c$ is usually very small, and the shear stress is almost zero during uplift, a constant $\gamma_c$ would suffice and is adopted in this paper. The effective stress-displacement relationship can be illustrated as Figure 5 and expressed as:

$$\boldsymbol{\sigma}' = \mathbf{D}\mathbf{d} \tag{8}$$

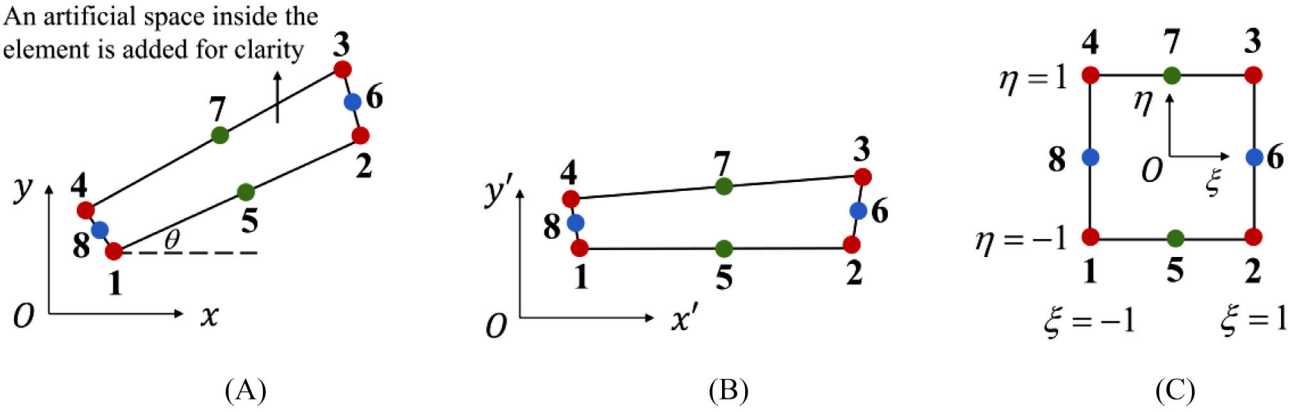


**FIGURE 6** The proposed eight-node interface element. (A) In original global coordinates. (B) In rotated global coordinates. (C) In local coordinates

where $\boldsymbol{\sigma}' = [\sigma'_n\ \sigma'_t]^T$ is the effective stress vector, and $\mathbf{d} = [g_n\ \gamma]^T$ the relative displacement vector. $\mathbf{D}$ is the stiffness matrix depending on relative shear displacement. Under compression, $\mathbf{D}$ reads:

$$\mathbf{D} = \begin{bmatrix} K_n & 0 \\ 0 & \dfrac{\nu K_n g_n}{\gamma_c} \end{bmatrix} (\gamma \le \gamma_c) \text{ or } \mathbf{D} = \begin{bmatrix} K_n & 0 \\ \dfrac{|\gamma|}{\gamma}\nu K_n & 0 \end{bmatrix} (\gamma > \gamma_c) \tag{9}$$

## 2.6 | Coupling between hydraulic and mechanical behaviours

Assuming the water to be incompressible, for a segment of the water-filled interface with opening $g_n$ and longitudinal width $\Delta x'$, its volumetric change equals the water flow-in volume minus the water flow-out volume:

$$\dot{g}_n \Delta x' = -v_{12}\Delta x' - v_{34}\Delta x' + \Delta q_x \tag{10}$$

where dot denotes material time derivative.

By using the divergence theorem, the mean value theorem of integrals, and letting $\Delta x' \to 0$, Equation (10) becomes:

$$-\frac{\partial q_x}{\partial x} + v_{12} + v_{34} + \dot{g}_n = 0 \tag{11}$$

# 3 | FORMULATION OF THE INTERFACE MODEL IN FINITE ELEMENT FRAMEWORK

## 3.1 | Element description

An eight-node element was constructed as shown in Figure 6. Note that the nodes 1, 4, 8, the nodes 5, 7, and the nodes 2, 3, 6 are co-located initially, and an artificial distance between them were added in this figure for clarity. Nodes $1 \sim 4$ have 3 degree of freedoms (DOFs): $x$, $y$ displacements and pore pressures at boundaries. Nodes 6 and 8 have DOF of pore pressure at mid-interface but no displacements DOF, while nodes 5 and 7 have displacements DOFs but no pore pressure DOF. The edge 1–2 in Figure 6 represents the boundary 1–2 in Figure 3, and the edge 3–4 represents the boundary 3–4. The longitudinal direction of the element is denoted as $Ox'$. The nodal coordinates of this interface are updated in real time according to their displacements during the analysis. The following formulation is based on straight geometries and curved geometry is not considered.

## 3.2 | Shape functions and interpolations

A local coordinate system $\xi O\eta$ is established to interpolate the field variables, as shown in Figure 6(C). The displacements are continuous along *x'* direction on boundaries 1–2 and 3–4 but discrete along *y'* direction. Thus, the displacements need to be interpolated separately on 1–2 and 3–4 as:

$$\begin{aligned}\mathbf{u_{12}} &= N_1\mathbf{u_1} + N_2\mathbf{u_2} + N_5\mathbf{u}_5\\ \mathbf{u_{34}} &= N_4\mathbf{u_4} + N_3\mathbf{u_3} + N_7\mathbf{u}_7\end{aligned} \tag{12}$$

where $\mathbf{u_{12}}$ and $\mathbf{u_{34}}$ are displacement vectors on 1–2 or 3–4; while $\mathbf{u_1} \sim \mathbf{u_7}$ are displacement vectors at nodes $1 \sim 7$ respectively. $N_i$ are one dimensional shape functions defined by the local coordinate $\xi \subseteq [-1, 1]$uniquely. The form that is the most widely adopted is:

$$N_1 = N_4 = \frac{\xi}{2}(\xi - 1)\,; N_2 = N_3 = \frac{\xi}{2}(\xi + 1)\,; \text{and } N_5 = N_7 = 1 - \xi^2 \tag{13}$$

Contrary to the displacements, the pore pressure is assumed continuous along both *x'* and *y'* directions, and thus its interpolation is a function of both $\xi$ and $\eta$. Considering that the distribution of pore pressure is longitudinally linear and transversely parabolic inside an element, following forms are proposed:

$$\begin{aligned}\bar{N}_1(\xi,\eta) &= \frac{1}{4}\eta(1-\xi)(\eta-1)\,; & \bar{N}_2(\xi,\eta) &= \frac{1}{4}\eta(1+\xi)(\eta-1)\\ \bar{N}_3(\xi,\eta) &= \frac{1}{4}\eta(1+\xi)(1+\eta)\,; & \bar{N}_4(\xi,\eta) &= \frac{1}{4}\eta(1-\xi)(1+\eta)\\ \bar{N}_6(\xi,\eta) &= \frac{1}{2}(1+\xi)(1-\eta)(1+\eta)\,; & \bar{N}_8(\xi,\eta) &= \frac{1}{2}(1-\xi)(1-\eta)(1+\eta)\end{aligned} \tag{14}$$

Accordingly,

$$p = \sum_{i=1}^{4}\bar{N}_i p_i + \bar{N}_6 p_6 + \bar{N}_8 p_8 \tag{15}$$

where $p$ is the pore pressure at $(\xi,\eta)$ and $p_i$ denotes pore pressure at the $i^{\text{th}}$ node.

For brevity, $N_{w1}$, $N_{w2}$ are used in the following derivation, which are defined as:

$$\begin{aligned}\bar{N}_{w1} &= \bar{N}_1 + \bar{N}_4 + \bar{N}_8 = \frac{1}{2}(1-\xi)\\ \bar{N}_{w2} &= \bar{N}_2 + \bar{N}_3 + \bar{N}_6 = \frac{1}{2}(1+\xi)\end{aligned} \tag{16}$$

## 3.3 | Matrix expressions of parameters

Let

$$\mathbf{N} = \begin{bmatrix}N_1 & N_2 & N_3\end{bmatrix}^T \tag{17}$$

$$\mathbf{u} = \begin{bmatrix}u_{1x} & u_{1y} & u_{2x} & u_{2y} & u_{3x} & u_{3y} & u_{4x} & u_{4y} & u_{5x} & u_{5y} & u_{7x} & u_{7y}\end{bmatrix}^T \tag{18}$$

$$\mathbf{R_N} = \begin{bmatrix}\sin\theta & -\cos\theta & 0 & 0 & 0 & 0 & -\sin\theta & \cos\theta & 0 & 0 & 0 & 0\\ 0 & 0 & \sin\theta & -\cos\theta & -\sin\theta & \cos\theta & 0 & 0 & 0 & 0 & 0 & 0\\ 0 & 0 & 0 & 0 & 0 & 0 & 0 & 0 & \sin\theta & -\cos\theta & -\sin\theta & \cos\theta\end{bmatrix} \tag{19}$$

and

$$\mathbf{R_T} = \begin{bmatrix} -\cos\theta & -\sin\theta & 0 & 0 & 0 & 0 & \cos\theta & \sin\theta & 0 & 0 & 0 & 0 \\ 0 & 0 & -\cos\theta & -\sin\theta & \cos\theta & \sin\theta & 0 & 0 & 0 & 0 & 0 & 0 \\ 0 & 0 & 0 & 0 & 0 & 0 & 0 & 0 & -\cos\theta & -\sin\theta & \cos\theta & \sin\theta \end{bmatrix} \tag{20}$$

where $\theta$ is the angle between $Ox$ and $Ox'$.

It follows that the relative displacements can be calculated as

$$\mathbf{d} = \begin{bmatrix} g_n \\ \gamma \end{bmatrix} = \begin{bmatrix} \mathbf{N^T} & \mathbf{0} \\ \mathbf{0} & \mathbf{N^T} \end{bmatrix} \begin{bmatrix} \mathbf{R_N} \\ \mathbf{R_T} \end{bmatrix} \mathbf{u} \tag{21}$$

where $\mathbf{u}$ is the nodal displacement vector in the global coordinate system $xOy$.

Combining Equation (21) with Equation (8), the effective stresses can be expressed as:

$$\boldsymbol{\sigma}' = \begin{bmatrix} \sigma'_n \\ \sigma'_t \end{bmatrix} = \mathbf{Dd} = \mathbf{D} \begin{bmatrix} \mathbf{N^T} & \mathbf{0} \\ \mathbf{0} & \mathbf{N^T} \end{bmatrix} \begin{bmatrix} \mathbf{R_N} \\ \mathbf{R_T} \end{bmatrix} \mathbf{u} \tag{22}$$

Similarly, let

$$\mathbf{p} = \begin{bmatrix} p_1 & p_2 & p_3 & p_4 & p_6 & p_8 \end{bmatrix}^T \tag{23}$$

$$\bar{\mathbf{N}} = \begin{bmatrix} \bar{N}_1 & \bar{N}_2 & \bar{N}_3 & \bar{N}_4 & \bar{N}_6 & \bar{N}_8 \end{bmatrix}^T \tag{24}$$

$$\bar{\mathbf{N}}_\mathbf{w} = \begin{bmatrix} \bar{N}_{w1} & \bar{N}_{w2} \end{bmatrix}^T \tag{25}$$

$$\mathbf{R_m} = \begin{bmatrix} \frac{1}{6} & 0 & 0 & \frac{1}{6} & 0 & \frac{2}{3} \\ 0 & \frac{1}{6} & \frac{1}{6} & 0 & \frac{2}{3} & 0 \end{bmatrix} \tag{26}$$

To calculate $\bar{p} - p_{12}$, a pore pressure difference matrix $\mathbf{R_b}$ is defined:

$$\mathbf{R_b} = \begin{bmatrix} -5 & 0 & 0 & 1 & 0 & 4 \\ 0 & -5 & 1 & 0 & 4 & 0 \end{bmatrix} \tag{27}$$

To calculate $\bar{p} - p_{34}$, a pore pressure difference matrix $\mathbf{R_t}$ is defined:

$$\mathbf{R_t} = \begin{bmatrix} 1 & 0 & 0 & -5 & 0 & 4 \\ 0 & 1 & -5 & 0 & 4 & 0 \end{bmatrix} \tag{28}$$

It follows that:

$$p = \bar{\mathbf{N}}^\mathbf{T}\mathbf{p}; \bar{p} = \bar{\mathbf{N}}_\mathbf{w}^\mathbf{T}\mathbf{R_m}\mathbf{p} \tag{29}$$

$$\bar{p} - p_{12} = \frac{1}{6}\bar{\mathbf{N}}_\mathbf{w}^\mathbf{T}\mathbf{R_b}\mathbf{p}; \bar{p} - p_{34} = \frac{1}{6}\bar{\mathbf{N}}_\mathbf{w}^\mathbf{T}\mathbf{R_t}\mathbf{p} \tag{30}$$

### 3.4 | Formulation of effective mechanical behaviours

The formulation of the mechanical behaviours follows the standard procedures of the principle of virtual work. For an arbitrary nodal displacement increment $\boldsymbol{\delta}\mathbf{u}$, the total work done by external forces, internal effective stresses, and pore pressure must be zero:

$$\int \boldsymbol{\delta}\mathbf{d}^{\mathrm{T}}\boldsymbol{\sigma}' dx' - \int p\delta V = \boldsymbol{\delta}\mathbf{u}^{\mathrm{T}}\mathbf{f} + \int \boldsymbol{\delta}\mathbf{d}^{\mathrm{T}}\boldsymbol{\sigma} dx' \tag{31}$$

where $\mathbf{f}$ and $\mathbf{u}$ are nodal concentrated force vector and nodal displacement vector in $xOy$, respectively; $\boldsymbol{\sigma}$ the external distributed load vector acting on boundaries; and $\boldsymbol{\sigma}$' the internal effective stress vector, $\mathbf{d}$ the relative displacement vector calculated in Equation (21).

For the second term on the left-hand side of Equation (31), the below relation holds:

$$\int p\delta V = \int \delta g_n \bar{p} dx' = \int \boldsymbol{\delta}\mathbf{u}^{\mathrm{T}}\mathbf{R}_{\mathbf{N}}^{\mathrm{T}}\mathbf{N}\bar{\mathbf{N}}_{\mathbf{w}}^{\mathrm{T}}\mathbf{R}_{\mathbf{m}}\mathbf{p} dx' \tag{32}$$

Similarly, replacing other variables in Equation (31) with their matrix forms, and considering that $\boldsymbol{\delta}\mathbf{u}^{\mathrm{T}}$, $\mathbf{u}$ and $\mathbf{p}$ are independent of coordinates, it becomes:

$$\begin{aligned}\boldsymbol{\delta}\mathbf{u}^{\mathrm{T}} \int \left( \begin{bmatrix} \mathbf{R}_{\mathbf{N}}^{\mathrm{T}} & \mathbf{R}_{\mathbf{T}}^{\mathrm{T}} \end{bmatrix} \begin{bmatrix} \mathbf{N} & \mathbf{0} \\ \mathbf{0} & \mathbf{N} \end{bmatrix} \mathbf{D} \begin{bmatrix} \mathbf{N}^{\mathrm{T}} & \mathbf{0} \\ \mathbf{0} & \mathbf{N}^{\mathrm{T}} \end{bmatrix} \begin{bmatrix} \mathbf{R}_{\mathbf{N}} \\ \mathbf{R}_{\mathbf{T}} \end{bmatrix} \right) dx' \mathbf{u} - \boldsymbol{\delta}\mathbf{u}^{\mathrm{T}} \int \left( \mathbf{R}_{\mathbf{N}}^{\mathrm{T}}\mathbf{N}\bar{\mathbf{N}}_{\mathbf{w}}^{\mathrm{T}}\mathbf{R}_{\mathbf{m}} \right) dx' \mathbf{p} \\ = \boldsymbol{\delta}\mathbf{u}^{\mathrm{T}}\mathbf{f} + \boldsymbol{\delta}\mathbf{u}^{\mathrm{T}} \int \left( \begin{bmatrix} \mathbf{R}_{\mathbf{N}}^{\mathrm{T}} & \mathbf{R}_{\mathbf{T}}^{\mathrm{T}} \end{bmatrix} \begin{bmatrix} \mathbf{N} & \mathbf{0} \\ \mathbf{0} & \mathbf{N} \end{bmatrix} \boldsymbol{\sigma} \right) dx'\end{aligned} \tag{33}$$

Equation (33) holds true for arbitrary $\boldsymbol{\delta}\mathbf{u}^{\mathrm{T}}$, so that $\boldsymbol{\delta}\mathbf{u}^{\mathrm{T}}$ can be cancelled from both sides. Thence, it finally becomes:

$$\mathbf{K}\mathbf{u} + \mathbf{L}\mathbf{p} = \mathbf{F} \tag{34}$$

where

$$\mathbf{K} = \int \left( \begin{bmatrix} \mathbf{R}_{\mathbf{N}}^{\mathrm{T}} & \mathbf{R}_{\mathbf{T}}^{\mathrm{T}} \end{bmatrix} \begin{bmatrix} \mathbf{N} & \mathbf{0} \\ \mathbf{0} & \mathbf{N} \end{bmatrix} \mathbf{D} \begin{bmatrix} \mathbf{N}^{\mathrm{T}} & \mathbf{0} \\ \mathbf{0} & \mathbf{N}^{\mathrm{T}} \end{bmatrix} \begin{bmatrix} \mathbf{R}_{\mathbf{N}} \\ \mathbf{R}_{\mathbf{T}} \end{bmatrix} \right) dx' \tag{35}$$

$$\mathbf{L} = -\int \left( \mathbf{R}_{\mathbf{N}}^{\mathrm{T}}\mathbf{N}\bar{\mathbf{N}}_{\mathbf{w}}^{\mathrm{T}}\mathbf{R}_{\mathbf{m}} \right) dx' \tag{36}$$

$$\mathbf{F} = \mathbf{f} + \int \left( \begin{bmatrix} \mathbf{R}_{\mathbf{N}}^{\mathrm{T}} & \mathbf{R}_{\mathbf{T}}^{\mathrm{T}} \end{bmatrix} \begin{bmatrix} \mathbf{N} & \mathbf{0} \\ \mathbf{0} & \mathbf{N} \end{bmatrix} \boldsymbol{\sigma} \right) dx' \tag{37}$$

$\mathbf{K}$ is the effective mechanical stiffness matrix relating displacements to effective mechanical stresses, and $\mathbf{L}$ is a hydro-mechanical coupling matrix relating displacements to pore pressures.

### 3.5 | Formulation of hydraulic behaviours

The formulation of hydraulic behaviour is based on Galerkin's method, and the transverse average pore pressure is used as trial function. One benefit of doing so is that it converts a 2D integration into 1D. By conducting integration by part, the weak forms of the continuity Equation (11) are Equation (38) for Darcy-like flow or Equation (39) for NS flow.

$$\frac{k_x}{\gamma_w} \left[ \int g_n \frac{\partial d\bar{p}}{\partial x'} \frac{\partial \bar{p}}{\partial x'} dx' \right] + \int d\bar{p} \left[ c_{12}(\bar{p} - p_{12}) + c_{34}(\bar{p} - p_{34}) + \frac{\partial g_n}{\partial t} \right] dx' = 0 \tag{38}$$

$$\frac{1}{120\mu}\left[\int g_n^3\frac{\partial d\bar{p}}{\partial x'}\left(8\frac{\partial p_g}{\partial x'}+\frac{\partial p_{12}}{\partial x'}+\frac{\partial p_{34}}{\partial x'}\right)dx'\right] + \int d\bar{p}\left[c_{12}\left(\bar{p}-p_{12}\right)+c_{34}\left(\bar{p}-p_{34}\right)+\frac{\partial g_n}{\partial t}\right]dx'=0 \tag{39}$$

Replacing the variables with their matrix forms, the two equations further become:

$$\mathbf{Gp}+\mathbf{H\dot{u}}=0 \tag{40}$$

where:

$$\frac{\partial\bar{\mathbf{N}}_\mathbf{w}}{\partial x'}=\begin{bmatrix}\frac{\partial\bar{N}_{w1}}{\partial x'} & \frac{\partial\bar{N}_{w2}}{\partial x'}\end{bmatrix}^T \tag{41}$$

$$\mathbf{H}=\int\left(\mathbf{R}_\mathbf{m}^\mathbf{T}\bar{\mathbf{N}}_\mathbf{w}\mathbf{N}^\mathbf{T}\mathbf{R}_\mathbf{N}\right)dx' \tag{42}$$

$$\mathbf{G}=\int\left(A\mathbf{R}_\mathbf{m}^\mathbf{T}\left(\frac{\partial\bar{\mathbf{N}}_\mathbf{w}}{\partial\mathbf{x}'}\right)\left(\frac{\partial\bar{\mathbf{N}}_\mathbf{w}}{\partial\mathbf{x}'}\right)^\mathbf{T}\mathbf{R}_\mathbf{F}\right)dx'+\frac{c_{12}}{6}\int\mathbf{R}_\mathbf{m}^\mathbf{T}\bar{\mathbf{N}}_\mathbf{w}\bar{\mathbf{N}}_\mathbf{w}^\mathbf{T}\mathbf{R}_\mathbf{b}dx'+\frac{c_{34}}{6}\int\mathbf{R}_\mathbf{m}^\mathbf{T}\bar{\mathbf{N}}_\mathbf{w}\bar{\mathbf{N}}_\mathbf{w}^\mathbf{T}\mathbf{R}_\mathbf{t}dx' \tag{43}$$

where A and $\mathbf{R_F}$ depends on the longitudinal flow type. For Darcy-like flow:

$$A=\frac{g_nK_x}{6\gamma_w}\text{and}\mathbf{R}_\mathbf{F}=\begin{bmatrix}1&0&0&1&0&4\\0&1&1&0&4&0\end{bmatrix} \tag{44}$$

while for NS flow:

$$A=\frac{g_n^3}{120\mu}\text{and}\mathbf{R}_\mathbf{F}=\begin{bmatrix}1&0&0&1&0&8\\0&1&1&0&8&0\end{bmatrix} \tag{45}$$

## 3.6 | Time integration and hydro-mechanical coupling matrix

$\dot{\mathbf{u}}$ in Equation (40) is the nodal displacement rate vector. Let $\mathbf{u^n}$ and $\mathbf{u^{n+1}}$ denote the nodal displacement vectors at time $t$ and $t+\Delta t$ respectively. Then, $\dot{\mathbf{u}}$ can be approximated as:

$$\dot{\mathbf{u}}=\frac{\mathbf{u^{n+1}}-\mathbf{u^n}}{\Delta t} \tag{46}$$

Meanwhile, $\mathbf{p}$ can be written as:

$$\mathbf{p}=(1-\alpha)\,\mathbf{p^{n+1}}+\alpha\mathbf{p^n} \tag{47}$$

where $\mathbf{p^n}$ and $\mathbf{p^{n+1}}$ are the nodal pore pressure vectors at time $t$ and $t+\Delta t$ respectively. $\alpha$ is an integration parameter ranging from 0 to 1, with $\alpha=0$ corresponding to implicit integration, $\alpha=1$ explicit integration, and $\alpha=0.5$ middle point integration.

Subjecting Equation (47) and (46) to (40), it becomes:

$$\Delta t\,(1-\alpha)\,\mathbf{Gp^{n+1}}+\mathbf{Hu^{n+1}}=\mathbf{Hu^n}-\Delta t\alpha\mathbf{Gp^n} \tag{48}$$

Equation (34) and (48) consist the *u-p* form of the proposed interface element, as summarised in Equation (49) where $\mathbf{u^n}$ and $\mathbf{p^n}$ are known while $\mathbf{u^{n+1}}$ and $\mathbf{p^{n+1}}$ are to be determined.

$$\begin{bmatrix} \mathbf{K} & \mathbf{L} \\ \mathbf{H} & \Delta t\,(1-\alpha)\,\mathbf{G} \end{bmatrix} \begin{bmatrix} \mathbf{u^{n+1}} \\ \mathbf{p^{n+1}} \end{bmatrix} = \begin{bmatrix} \mathbf{F} \\ \mathbf{Hu^n} - \Delta t\alpha \mathbf{Gp^n} \end{bmatrix} \tag{49}$$

This time integration scheme is the same as in Small et al.[26] and has proved to be unconditionally stable when $\alpha > 0.5$.

## 4 | NUMERICAL IMPLEMENTATIONS OF THE INTERFACE

### 4.1 | Jacobian parameter

The calculation of matrices in Equation (49) needs to integrate functions of $\xi$ with respect to global coordinate $x$'. Therefore, the Jacobian matrix which reduces to a scalar in 1D cases (called Jacobian parameter in this paper) is needed for coordinate transformation. In this case, its definition is $dx' = |J|d\xi$, where $J$ is the Jacobian parameter, and '| |' means absolute value. Thus, the Jacobian parameter can be determined as (choosing the surface 1–2 as the reference surface):

$$|J| = \frac{\partial x'}{\partial \xi} = \frac{dN_1}{d\xi}x'_1 + \frac{dN_2}{d\xi}x'_2 + \frac{dN_5}{d\xi}x'_5 \tag{50}$$

where $x'_1$, $x'_2$ and $x'_5$ are the $x$' coordinates of nodes 1, 2 and 5, respectively.

### 4.2 | Gauss points

It is reported that the Newton-Cotes integration scheme is better than the conventional Gauss integration scheme for zero-thickness elements, because the latter may result in oscillations of the results when the interface shearing is dominant.[3–27] This study mainly considers uplifting problems where shearing is not involved. Thus, Gauss integration was employed, and it showed a robust performance in this study. Two Gauss points located at $\xi = \pm 1/\sqrt{3}$ were chosen, the weight being unity for both points.

### 4.3 | Newton-Raphson method

After calculating matrices in Equation (49), Newton-Raphson method can be employed to solve it at each time step by performing following iterations, where the superscript denotes the $n^{th}$ time step and the subscript denotes the $m^{th}$ iteration at this time step.

$$\begin{bmatrix} \mathbf{K^n} & \mathbf{L^n} \\ \mathbf{H^n} & \Delta t\,(1-\alpha)\,\mathbf{G^n} \end{bmatrix} \begin{bmatrix} \mathbf{\Delta u^n_m} \\ \mathbf{\Delta p^n_m} \end{bmatrix} = \begin{bmatrix} \mathbf{K^n} & \mathbf{L^n} \\ \mathbf{H^n} & \Delta t^n\,(1-\alpha)\,\mathbf{G^n} \end{bmatrix} \begin{bmatrix} \mathbf{u^n_m} \\ \mathbf{p^n_m} \end{bmatrix} - \begin{bmatrix} \mathbf{F^n} \\ \mathbf{H^n u^n} - \Delta t^n \alpha \mathbf{G^n p^n} \end{bmatrix}$$
$$\begin{bmatrix} \mathbf{u^n_{m+1}} \\ \mathbf{p^n_{m+1}} \end{bmatrix} = \begin{bmatrix} \mathbf{u^n_m} \\ \mathbf{p^n_m} \end{bmatrix} + \begin{bmatrix} \mathbf{\Delta u^n_m} \\ \mathbf{\Delta p^n_m} \end{bmatrix} \tag{51}$$

When the $\mathbf{[\Delta u^n{}_m\ \Delta p^u{}_m]^T}$ is less than the targeted precision, above iterations are terminated, the variables are updated as $\mathbf{[u^{n+1}{}_1\ p^{u+1}{}_1]^T = [u^n{}_m\ p^u{}_m]^T}$, and the calculation marches on to the $n$+1$^{th}$ time step. In displacement FE, the initial values of the variables at the first time step are usually $\mathbf{[u^1{}_1\ p^1{}_1]^T = 0.}$

Note that Equation (51) is just for a single interface element. In the later modelling, it will be assembled with into global stiffness matrix soil elements.

**TABLE 1** Parameters of the interface model

| | Parameters input for the interface | values | Flow types |
|---|---|---|---|
| Mechanical parameters | Normal stiffness $K_n$: kPa/m | $10^9$ (in contact)<br>0.1 (not in contact) | Both Darcy-like and NS |
| | Critical shear displacement $\gamma_c$: m | 0.001 | |
| | Parameter of friction of interface $\nu$ | 0.35 (in contact)<br>0.01 (not in contact) | |
| | Hydraulic conductivity $c_{12}$: m/(kPa•s) | $1\times10^{-9}$ | |
| Hydraulic parameters | Hydraulic conductivity $c_{34}$: m/(kPa•s) | 0 | |
| | Longitudinal conductivity $K_x$: m/s | $1\times10^{-9}$ | Darcy-like only |
| | Interface fluid viscosity μ (Pa•s) | $1\times10^{2}$ | NS only |

## 5 | DISCUSSION OF THE INTERFACE PARAMETERS

The proposed interface model has seven parameters in total, as summarised in Table 1. They can be divided into mechanical and hydraulic parameters. The mechanical parameters include the normal stiffness $K_n$, the friction coefficient $\nu$, and the critical shear displacement $\gamma_c$. The hydraulic parameters include transverse hydraulic conductivities $c_{12}$ and $c_{34}$, and the longitudinal conductivity $K_x$ (Darcy-like flow) or the interface fluid viscosity μ (NS flow). The last two parameters are used exclusively, and therefore only 6 parameters are needed in the modelling.

The normal stiffness $K_n$ is taken as $1\times10^9$ kPa/m when the structure and soil are in contact to prevent over-penetration, while it changes to a small number (0.1 kPa/m instead of 0 to keep numerical stability) when the structure and soil are separated. The coefficient of friction $\nu$ is taken as 0.35 when the structure and the soil are in contact. When they are separated, it is taken as 0.01(instead of 0 to keep numerical stability). The critical shear displacement $\gamma_c$, which is the boundary between elastic and plastic sliding, was considered as 0.001 m, following Ref. 16. In modelling uplift, the effective stresses within the interface are negligible, and thus the three mechanical parameters have relatively minor influences on the results. Therefore, no sensitivity study is undertaken for these parameters.

$c_{12}$ is the description of the micro-structure and intrinsic permeability of the boundary 1–2. Its dimension is $L^2T/M$ (with unit of m/(Pa•s)), meaning fluid flow rate under unit pressure difference. The values of $c_{12}$ in the literature vary significantly depending on the type of soils and problems investigated. For example, Cerfontaine et al.[28] used 1 m/(kPa•s) for sand, while Hu et al.[29] used $1.28\times10^{-10}$ m/(kPa•s) for leachate flow in waste fills. In the following simulation, a value of $c_{12} = 1\times10^{-9}$ m/(kPa•s) was adopted by calibrating against the tests in Figure 1.[10] This value is consistent with[29] for low permeability soils. $c_{34}$ was adopted as 0 because the structure in this paper was considered impermeable.

The Darcy-like longitudinal conductivity of the interface $K_x$ was considered constant for simplicity, and it was taken the same as the soil permeability, which was believed to represent reasonably a buried structure where the longitudinal flux comes solely from the soil. For the NS longitudinal flow, the fluid viscosity μ inside the interface was first taken as $1\times10^{-3}$ Pa•s, which is the viscosity of pure water at 20 ˚C. It was found that, with this value, the model significantly underestimated the uplift resistance compared with experimental data (as shown in Figure 11), indicating an overprediction of the fluid flow at the interface by the NS flow model. This is because the fluid flow in the experiment is predominantly a Darcy-like flow at the initial stage of uplifting when the footing is in contact with the soil. Thus, in order to use NS flow to realise the simulation (keeping in mind breakaway cannot be modelled with a Darcy-like flow), a much larger 'artificial' fluid viscosity value is required. This large fluid viscosity represents an equivalent value during the whole process, rather than an accurate estimation of pure fluid. A best-fit viscosity value of $1\times10^2$ Pa•s was obtained in this study and Figure 11 shows the comparison with experiments.

The sensitivities of the three parameters $c_{12}$, $K_x$ and μ are discussed later.

## 6 | CALCULATION EXAMPLE: UPLIFT OF A SURFACE FOOTING

### 6.1 | General introduction

In this section, the proposed interface along with soil elements was used to simulate the uplift of a surface footing at varying rates. Both Darcy-like and NS longitudinal flows were considered.

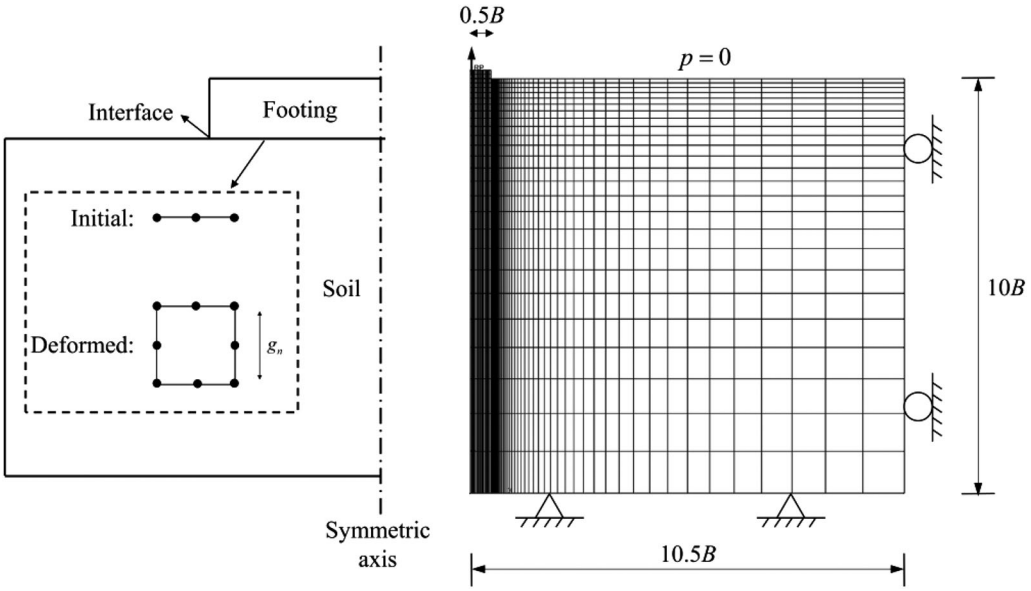


**FIGURE 7** Numerical model setup and mesh for surface footing uplift

## 6.2 | Model setup

The problem was considered as plane strain for simplicity. Due to symmetry, only a half model was established (Figure 7), including the footing, the interface, and the underlying soil, where the interface was a single layer of the proposed element with an initial thickness of 0. The interface was tied to the soil top surface and the footing, and stresses and pore pressures were shared at the overlapping nodes. Mesh sensitivity study was conducted, and the model shown in Figure 7 was demonstrated adequate. The meshes around the footing corner was 0.05*B*, where *B* is the width of the footing.

The boundary conditions are as follows: displacements of the soil bottom were not allowed, while two lateral sides can move vertically. No displacement constraint was applied to the top, and it was considered as a free drainage boundary except for the contacting part with the footing. The right side of the interface (i.e. the entrance for the ambient water) was set as free drainage boundary to enable longitudinal flow. In order to facilitate results interpretation, the soil was assumed weightless and uniform, with a surcharge of $\sigma'_v = 200$ kPa applied on the top surface.

The soil adopted the Modified Cam Clay (MCC) constitutive model.[30,31] In this model, the soil elastic behaviour obeys porous elasticity:

$$\begin{bmatrix} \delta\varepsilon_V^e \\ \delta\varepsilon_q^e \end{bmatrix} = \begin{bmatrix} \frac{1}{K} & \\ & \frac{1}{3G} \end{bmatrix} \begin{bmatrix} \delta p' \\ \delta q \end{bmatrix} \tag{52}$$

where $p$' is the effective mean stress, $q$ the deviatoric stress, $K$ the bulk modulus, $G$ the shear modulus, ${\varepsilon_v}^e$ the elastic volumetric strain and ${\varepsilon_q}^e$ the elastic deviatoric strain.

The yield surface of MCC is an ellipse in $p$'-$q$ space and can be expressed as:

$$f = q^2 - M^2\left[p'\left(p_0 - p'\right)\right] = 0 \tag{53}$$

where $M$ is the slope of the critical state line, and $p_0$ the right vertex of the ellipse.

Associated flow was assumed, and the magnitude of $p_0$ evolves with plastic volumetric strain according to:

$$\delta {p_0}' = \frac{(1+e)\,p_0}{(\lambda-\kappa)}\delta\varepsilon_V^p \tag{54}$$

**TABLE 2** Parameters for MCC constitutive model

| Parameters input for finite-element analysis | Values |
|---|---|
| Permeability of soil, $k$: m/s | $1.0\times10^{-9}$ |
| Slope of swelling and recompression line $\kappa$ | 0.044 |
| Slope of virgin compression line $\lambda$ | 0.205 |
| Slope of critical state line, $M$ | 0.92 |
| Friction angle in triaxial compression, $\varphi$ | 23.5° |
| Void ratio on critical state line with effective mean stress equals 1 kPa, $e_{cs}$ | 2.14 |

where $e$ is the void ratio, $\lambda$ and $\kappa$ the slopes of the virgin consolidation line and unloading-reloading line, respectively, and $\varepsilon_v{}^p$ the plastic volumetric strain.

Water flow inside the soil was considered obeying Darcy's law, and it was combined with MCC model and Biot's consolidation theory[32] to enable coupled analysis. The hydro-mechanical coupling equation of the soil can thus be expressed as:

$$\frac{\partial \varepsilon_V}{\partial t} = \frac{k}{\gamma_w}\left(\frac{\partial^2 p}{\partial x^2} + \frac{\partial^2 p}{\partial y^2} + \frac{\partial^2 p}{\partial z^2}\right) \tag{55}$$

where $\varepsilon_v$ is the total volumetric strain, $t$ the physical time, $k$ the soil permeability, assumed homogeneous at all directions, $p$ the excess pore pressure and $x$, $y$, $z$ three orthometric directions of the space. $\gamma_w$ is the unit weight of water, taking as 10 kN/m$^3$, which is required in Darcy's law.

A detailed description of how coupled analysis is realised for MCC using finite element method can be found in Ref. 26 and thus is not repeated here.

Typical MCC soil parameters for commercially available kaolin clay were adopted in this paper (see Table 2, based on the study of Stewart[33]). The soil strength was uniform and can be calculated by[34]:

$$s_u = \frac{\sigma'_v}{\sqrt{3}}\frac{\sin\varphi}{a}\left(\frac{a^2+1}{2}\right)^{(\lambda-\kappa)/\lambda} = 57.2\text{kPa} \tag{56}$$

where $\varphi$ is the frictional angle of soil, $\lambda$ the slope of normal consolidation line of soil, $\kappa$ the slope of unloading-reloading line, and $a = (3\text{-}\sin\varphi)/(6\text{-}4\sin\varphi)$.

## 6.3 | Results interpretation

The numerical results were presented using dimensionless parameters. The uplift displacement was normalised as $w/B$, where $w$ is the vertical displacement of footing and $B$ the width of footing. The rate was normalised using the widely adopted expression in compression problems $V = vB/c_v$,[35] where $v$ is the uplift velocity of the footing; $c_v = k(1+e_0)\sigma_v{}'/\lambda\gamma_w$ the coefficient of consolidation of the soil; $k$ the permeability; $e_0$ the initial void ratio; and $\sigma'_v$ the effective surcharge of the soil. The uplift resistance was normalised as $F/Bs_u$, where $F$ is the uplift force. $N_c = F_{\max}/Bs_u$ is the uplift capacity factor with $F_{\max}$ denoting the peak uplift resistance. The transverse and longitudinal flow velocities were normalised as $q_y/vB$, and $q_x/vB$, where $q_x$ and $q_y$ are the longitudinal flux and transverse flux, respectively.

The uplift was simulated by displacing the footing $0.5B$ vertically at normalised velocities $V$ = 30000, 3000, 300, 30, 3, 0.3 and 0.03, respectively. For each velocity, both Darcy-like and NS longitudinal flows were considered. In addition, $V = 3\times10^{10}$ was conducted for the NS flow type.

The $N_c$ for fully drained cases (slow uplift) is expected to be 0 because there is no suction throughout. For fully undrained cases (fast uplift), a reverse end bearing mechanism is expected, and the $N_c$ is the same as that under compression, of which the exact solution is $2+\pi$ for a surface footing on homogeneous cohesive soil.[36,37] Above two limits were used to verify the numerical results.

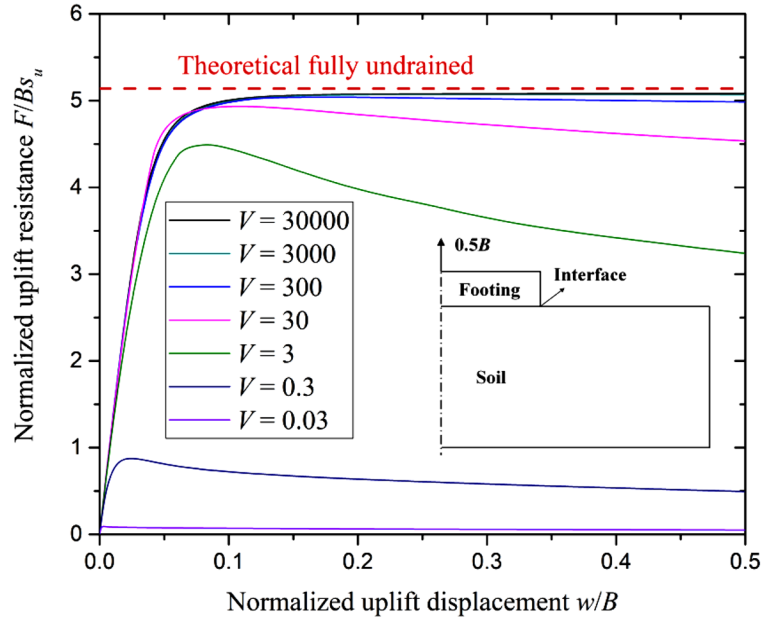


(A) Normalized uplift resistance-displacement curves

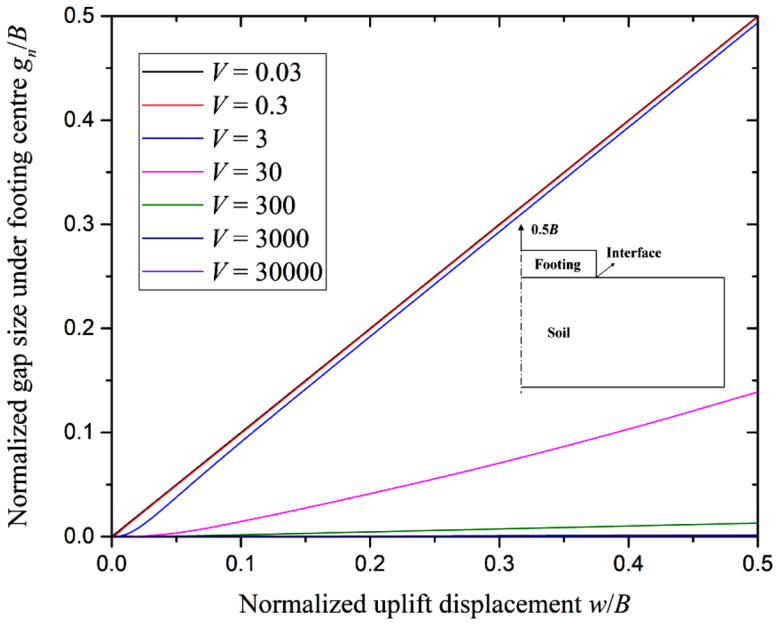


(B) Normalized interface thickness-displacement relationships

**FIGURE 8** Numerical results for Darcy-like flow type. (A) Normalised uplift resistance-displacement curves. (B) Normalised interface thickness-displacement relationships

### 6.3.1 | Darcy-like flow type

Figure 8(A) and (B) show the development of uplift resistance and interface thickness against uplift displacement, respectively. For $V \geq 300$, the peak uplift resistance $N_c$ is close to the exact solution $2+\pi$, with interface thickness negligible throughout. With the uplift rate diminishing, $N_c$ decreases, and interface thickness increases. But the interface thickness is always less than the footing displacement, indicating that the soil was partially attached to the footing. At $V = 0.03$, $N_c$ is close to zero. The interface thickness equals the uplift displacement at any instant, indicating non-attachment between footing and soil.

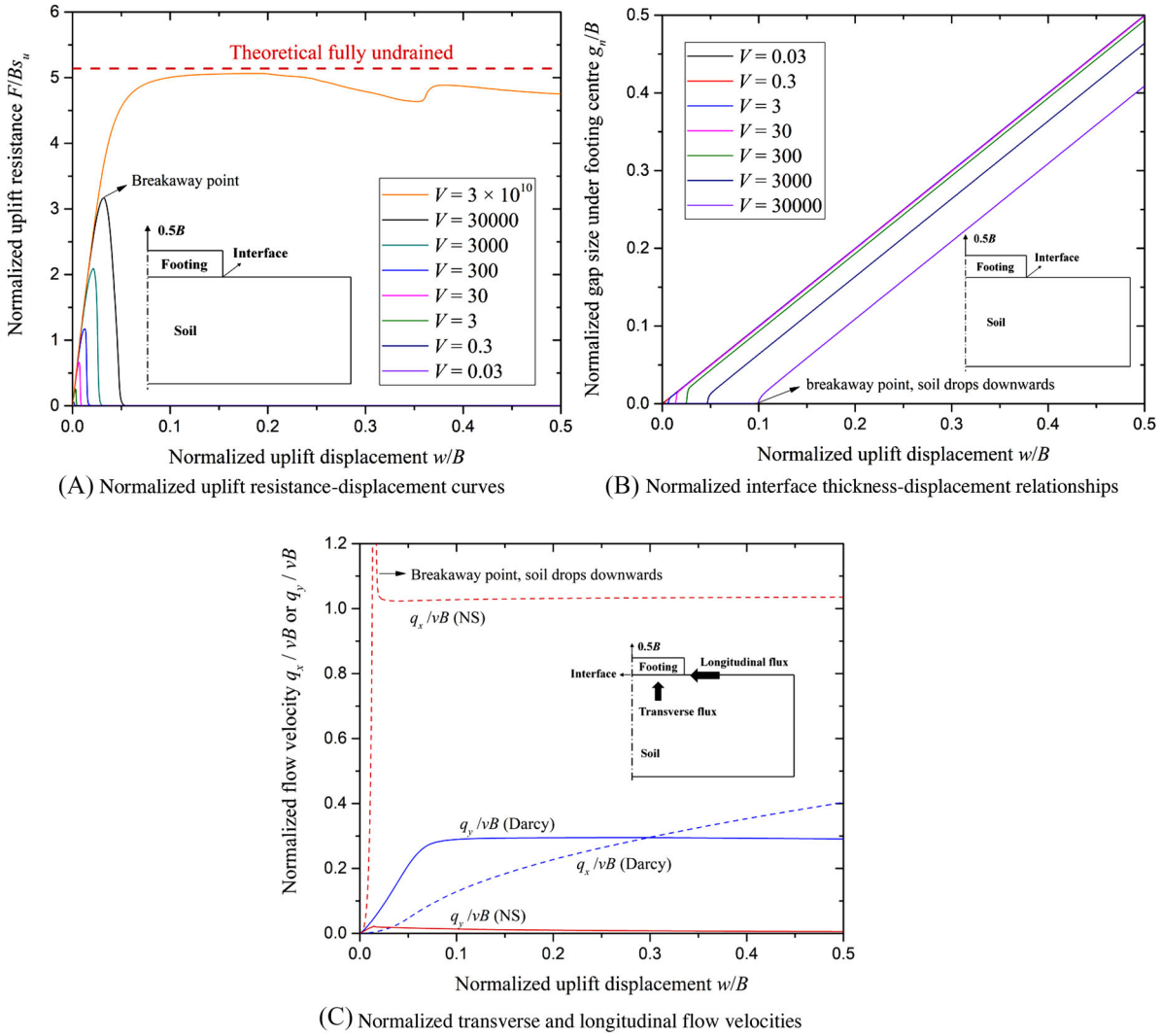


**FIGURE 9** Numerical results for NS flow type. (A) Normalised uplift resistance-displacement curves. (B) Normalised interface thickness-displacement relationships. (C) Normalised transverse and longitudinal flow velocities

### 6.3.2 | NS flow type

Figure 9 shows the results for NS flow type. It can be seen that NS type reaches fully undrained condition at $V = 3{\times}10^{10}$, 7 orders of magnitude greater than the Darcy-like flow type. Its most obvious difference from Darcy-like type is that breakaway occurred during the uplift, as reflected by the sudden drop in uplift resistance in Figure 9(A) and a drastic increase of interface thickness in Figure 9(B). These differences with Darcy-like type are because the NS equations, which do not consider the flow resistance from soil skeleton, predict faster water flow than Darcy's law, as is confirmed in Figure 9(C), leading to faster post-peak suction dissipation.

## 6.4 | Discussion and comparison with experimental observations

Figures 8 and 9 demonstrate that this interface allows the uplift rate, drainage condition, suction, interface opening, and water flow to be coupled in a compatible and automatic way. Slow uplift rates correspond to drained conditions where suction is not generated at the footing underside. Correspondingly, the soil does not move, and thus a gap is formed as water flowing in, with the opening rate equals the uplift rate. Higher uplift rates correspond to partially drained conditions, with some suction generated within the interface, drawing the soil partially up. Correspondingly, the interface thickness increase rate is less than the uplift rate. In this case, a post-peak softening of uplift resistance can be observed, which is

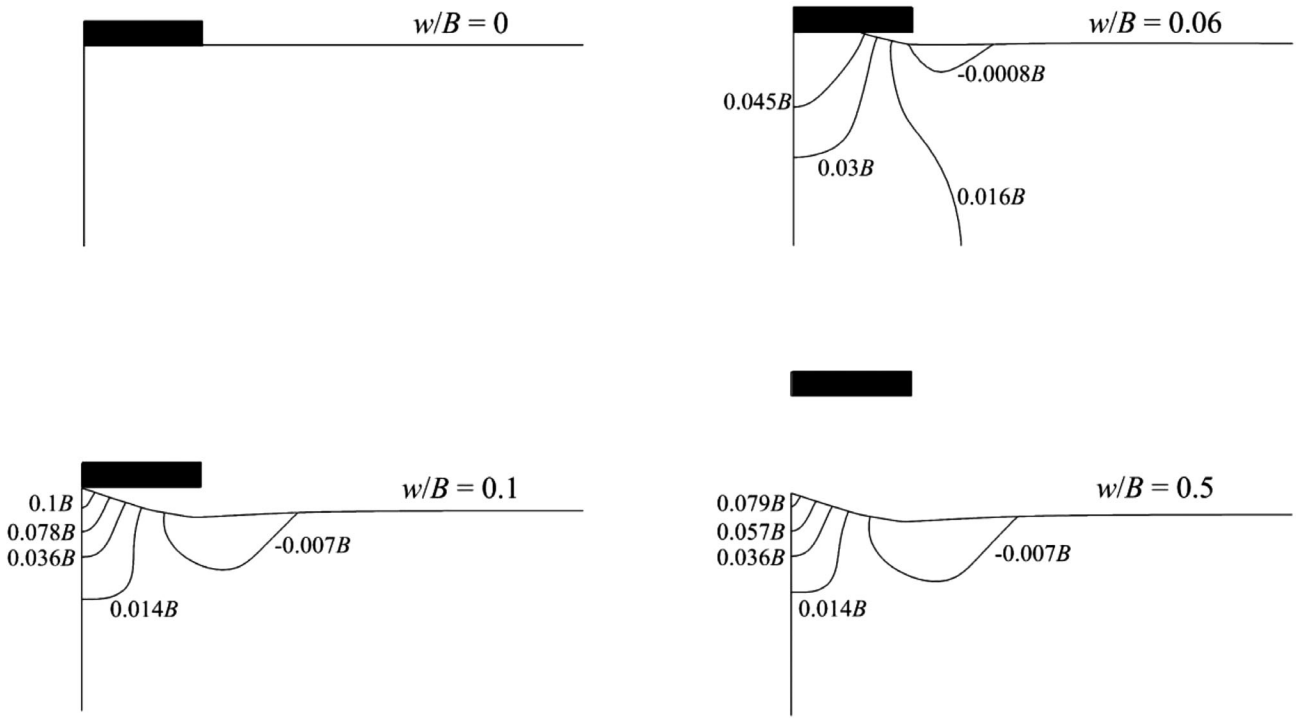


**FIGURE 10** Ground vertical displacement contours for NS flow type at $V = 30{,}000$

believed due to the suction dissipation induced by longitudinal and transverse flows. The significance of this softening is mild in Darcy-like type but drastic in NS type, due to the difference in longitudinal flow rates in the two types. Fast rates correspond to undrained conditions, where water flow-in is negligible. Thus, the gap does not open, and suction does not have time not dissipate. Correspondingly, a reverse end bearing failure mechanism occurs, and the numerical uplift capacity equals the exact solution. Above analyses demonstrate that this interface is able to (1) reproduce hydro-mechanical coupled uplift behaviours, and (2) precisely predict uplift resistance.

It is interestingly noted that in the partially drained uplift tests of shallow foundations, the uplift resistance first undergoes a mild post-peak softening which resembles that in Darcy-like type (Figure 8A, $0.3 \leq V \leq 30$), followed by a sudden breakaway which is captured by the NS type (Figure 9A). Based on this, the breakaway can be explained as a sudden increase of water flux into the foundation underside (considering the NS equations predict much higher longitudinal flow rate than Darcy's law) as the foundation was pulled out of soil.

Li[10] conducted PIV tests and observed that the soil underneath the foundation moved downwards as breakaway occurred. This is captured in Figure 9(B), where the slopes of $g_n/B - w/B$ curves are greater than 1 at breakaway points. This means the interface thickness increase rate exceeded the uplift rate at this moment, indicating the soil dropped down. This drop-down was because the underlying soil underwent unloading as the suction acting on it was quickly lost.

This soil drop-down can be observed in Figure 10 more evidently, which shows the ground vertical displacement contours of NS type at $V = 30{,}000$. It can be seen that the interface started opening from the footing edge, which was the entrance of free water and propagated towards the footing centre. Before $w/B = 0.1$ where breakaway initiated, the footing centre kept contacting the soil while the edge separated from it. Afterwards, the soil slightly moved down, and the footing was completely separated from the soil.

## 7 | BACKBONE CURVES

### 7.1 | Comparison with available studies

Lehane et al.[38] conducted centrifuge tests about foundation uplift at varying rates at 50 g. The foundation was buried in soil, with clay underneath and sand above the foundation. As the sand was substantially in drained conditions, it can be

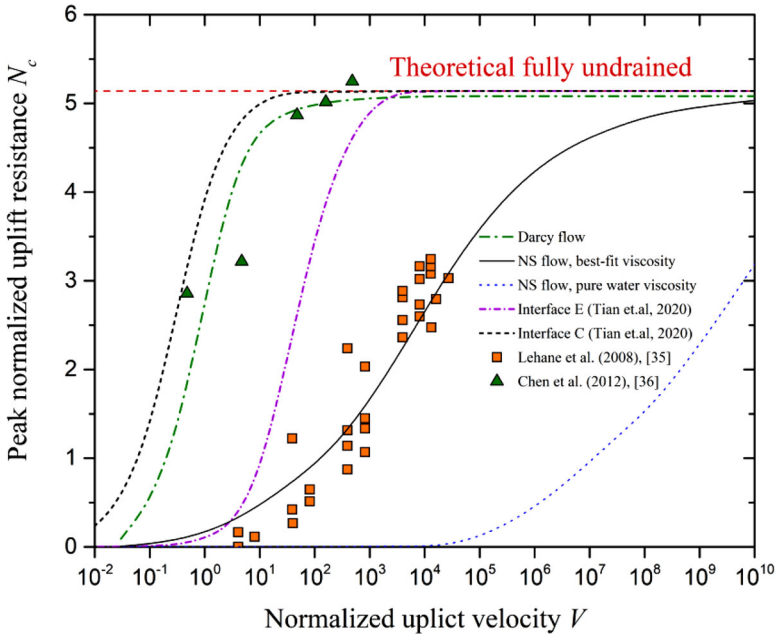


**FIGURE 11** Comparison of $N_c - V$ backbone curves of two flow types with experimental data and numerical solutions

deemed as a surface footing with surcharge. Chen et al.[39] conducted centrifuge tests at 150 g by using a surface footing directly sitting on the soil surface with no surcharge applied. In both studies, the footings were of comparable size, and the clay samples were the same commercially available kaolin, intensively characterised at the University of Western Australia.

These data, along with some available numerical solutions, are compared with above numerical results in Figure 11. Interestingly, the NS backbone curve using the best-fit viscosity reproduces with reasonable accuracy the trend in Lehane et al.,[38] while the Darcy-like backbone curve matches well with the results of Chen et al.[39] The discrepancy between the two groups of test data may come from a common experimental stage where the soil was allowed to consolidate under the self-weight of the foundation before uplift, which is expected to cause the foundation slightly penetrating the soil. Considering that the acceleration in Lehane et al.[38] was three times larger than in Chen et al.,[39] making the foundation of the former heavier in prototype, the footing in Chen et al.[39] would be expected to have deeper penetration. Thus, the longitudinal flow in Chen et al.[39] was hindered by the soil, such that the Darcy-like flow is more appropriate to estimate the results.

## 7.2 | Sensitivity of parameters of the interface

Sensitivity studies of the three hydraulic parameters (the hydraulic conductivity $c_{12}$, the longitudinal conductivity $K_x$ and the fluid viscosity μ) were conducted. A total of 121 cases were performed with varying $c_{12}$, $K_x$ or μ. All other parameters were kept constant unless otherwise stated.

The influence of $c_{12}$ is shown in Figure 12, where the Darcy-like longitudinal conductivity $K_x$ was set to 0 to suppress longitudinal flow. It is interesting to note that as $c_{12}$ increases 1 order of magnitude, the backbone curve translates rightwards roughly 1 order of magnitude. This is because the transverse flow is increased proportionally, and it is the only dominant factor to dissipate suction in this case. The influence of $K_x$ is presented in Figure 13, where the backbone curve moves leftwards as $K_x$ decreases. However, the backbone curve converges to the $K_x = 1{\times}10^{-9}$ m/s curve as $K_x$ further decreases. This means that, below this value, the longitudinal flow becomes negligible compared with transverse flow. The influence of μ is shown in Figure 14, where the increase of μ leads to leftwards movement of the backbone curve. The influence of μ is most significant in the middle of the backbone curve. At the two ends, this influence is insignificant. Note that the results in Figure 14 are from NS flow only.

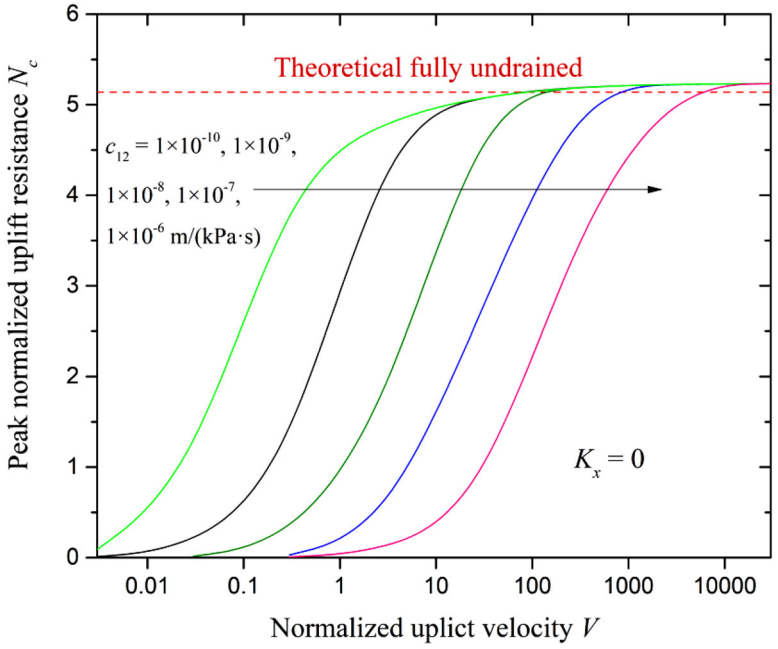


**FIGURE 12** Influence of $c_{12}$ on backbone curves

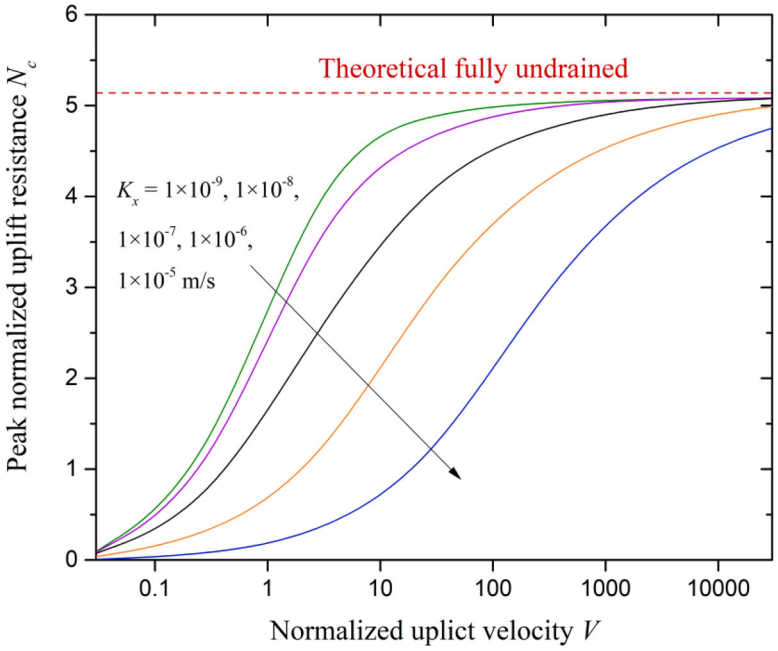


**FIGURE 13** Influence of $K_x$ on backbone curves

## 7.3 | A new perspective on the backbone curve

The discrepancy between the experimental data in Figure 11 implies that the widely adopted dimensionless velocity in compression cases $V = vB/c_v$[10,35,38,39] may not be adequate for uplifting problems, due to the existence of longitudinal and transverse flows. A more reasonable normalisation is to compare the water flow-in rate with uplift rate. Based on this, this paper proposes a new dimensionless velocity:

$$\bar{V} = \frac{v}{\left[\beta(c_{12}\gamma_w B)^{\alpha} + (1-\beta)K_x^{\alpha}\right]^{\frac{1}{\alpha}}} \tag{57}$$

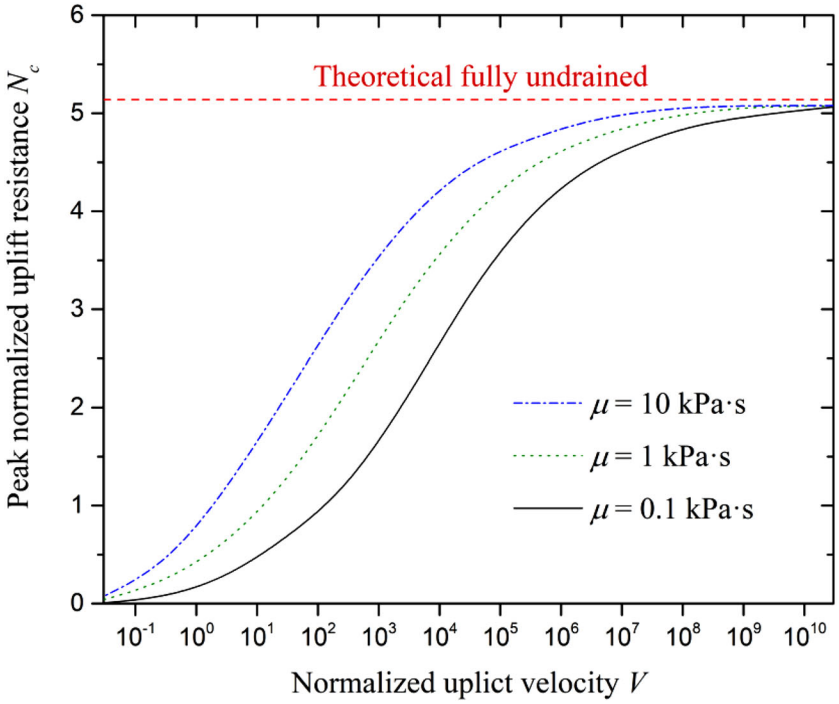


**FIGURE 14** Influence of $\mu$ on backbone curves

where $\alpha$ and $\beta$ are two to-be-fit parameters. For NS longitudinal flow, the $K_x$ term can be approximated by (according to cubic law):

$$k_x = \frac{g_{n0}^2 \gamma_w}{12\mu} \tag{58}$$

where $g_{n0}$ is a representative interface thickness.

Adopting the best-fit values $\alpha = 0.5, \beta = 0.5$ and $g_{n0} = 0.008$ m, the uplift rates of all above numerical data are normalised using Equation (57), and the results are shown in Figure 15. It can be observed that these data distribute closely around an average curve for different values of $c_{12}$ and $K_x$ or μ, and this average backbone curve can be estimated by a least-square best fit in the form of:

$$\frac{N_c}{N_{c,\text{undrained}}} = a + \frac{b}{1 + c\bar{V}^d} \tag{59}$$

where $N_{c,\text{undrained}} = \pi + 2$; and $a = 0$, $b = 1$, $c = 8.82$ and $d = -0.74$ are determined by least-square best fit.

## 8 | CONCLUDING REMARKS

A hydro-mechanical coupled zero thickness interface was proposed with full details of the physics-based constitutive relations. Complete FE formulation and implementation were presented based on an 8-node element.

The performance of the proposed interface was demonstrated by simulating the uplift of a surface footing at varying rates. By compatibly addressing suction generation/dissipation and structure-soil separation, the rate effect can be modelled without user intervention. If NS longitudinal flow is employed, breakaway can be simulated (note that any zero-thickness element which can incorporate a NS longitudinal flow would be able to simulate the breakaway). A new dimensionless velocity was proposed to better normalise uplift rate, accounting for the influence of transverse and longitudinal flows, and a unified backbone curve was established correspondingly. In general, the interface model in this study is capable of modelling the structure-soil interface behaviour during uplifting problems. It should also be noted that uplifting objects off seabed is extremely challenging to be precisely modelled and the model parameters in this paper need further validation from physical modelling, which is seen as the next step for future study.

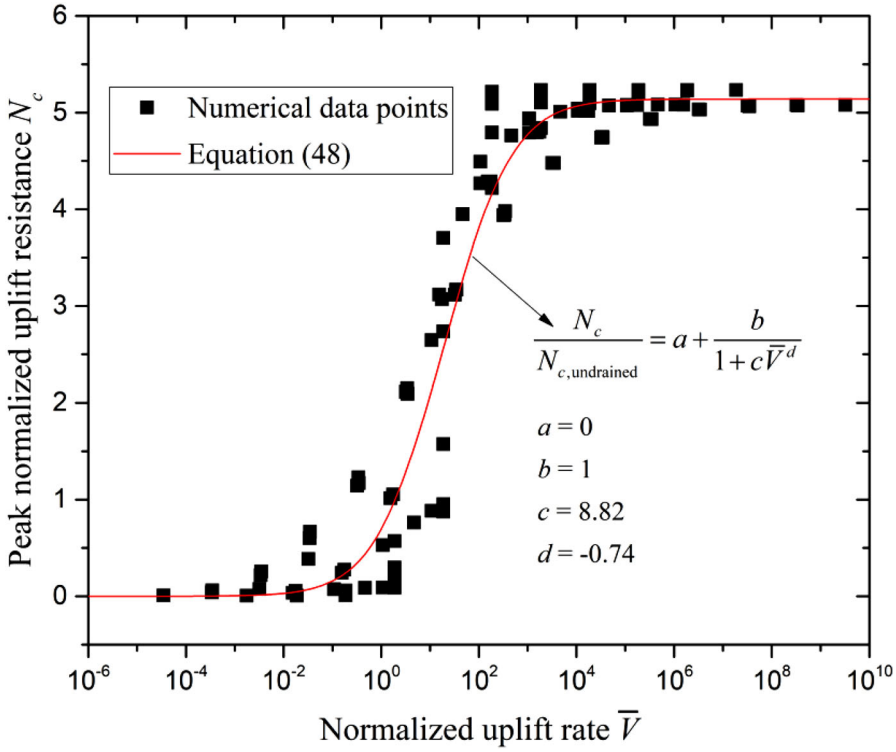


**FIGURE 15** New normalisation to numerical data points and best-fit backbone curve

**FIGURE 16** Force balance condition of a fluid element for NS flow

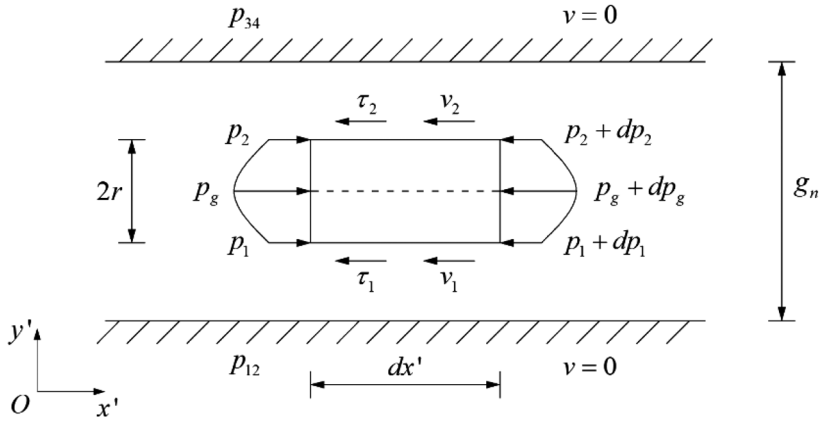


## NOMENCLATURE

| | |
|---|---|
| $\bar{N}_1 \sim \bar{N}_8$ | Shape functions for excess pore pressure |
| $\bar{V}$ | Newly proposed dimensionless uplift rate |
| $\bar{N}_{w1}$ and $\bar{N}_{w2}$ | Synthesized shape functions for excess pore pressure |
| μ | Fluid viscosity |
| A | Coordinate transformation matrix |
| $a_{w1}$, $a_{w2}$ | Transfer coefficients at surfaces 1–2 and 3–4 |
| $B$ | Surface footing width |
| $c_{12}$, $c_{34}$ | Hydraulic conductivities of the interface |
| $c_v$ | Coefficient of consolidation of the soil |
| D | Consistent stiffness matrix of the interface |
| d | Relative displacement vector of the interface |
| $e_0$ | Initial void ratio |

| | |
|---|---|
| $e_{cs}$ | Void ratio at $p' = 1$ kPa on critical state line |
| $F$ | Uplift force |
| $G$ | Shear modulus of soil |
| $g_n$ | Interface thickness between structure and soil |
| $J$ | Jacobian parameter |
| $k$ | Permeability of soil |
| $K$ | Bulk modulus of soil |
| $K_0$ | Coefficient of the earth pressure |
| $k_{g1}, k_{g2}$ | Intrinsic permeabilities rates at surfaces 1–2 and 3–4 |
| $K_{\mathrm{n}}$ | Normal stiffness in mechanical contact |
| $K_x$ | Longitudinal conductivity of interface |
| $M$ | Slope of critical state line |
| n | Outside normal of boundaries |
| $N_1, N_2, N_3$ | Shape functions for displacement |
| $N_c$ | Bearing capacity factor |
| $N_c$* | Theoretical undrained uplift capacity of a surface footing |
| $p$' | Effective mean stress of soil |
| $p, \bar{p}$ | Pore pressure and average pore pressure |
| $p_0$ | Size of the soil yield surface |
| $p_{12}, p_{12}, p_g$ | Pore pressures at surface 1–2, 3–4 and mid-interface |
| $q$ | Deviatoric stress of soil |
| $q_x, q_y$ | Longitudinal and transverse flux |
| $r$ | Vertical distance to mid-interface |
| $\mathrm{S_T}, \mathrm{S_D}, \mathrm{S_P}, \mathrm{S_V}$ | Stress, displacement, pore pressure and velocity boundaries |
| $s_{\mathrm{u}}$ | Undrained shear strength |
| T | Interface-soil total stress tensor |
| $t$ | Time |
| u, $\bar{\mathbf{u}}$ | Displacement and predefined displacement vectors |
| $V$ | Dimensionless uplift rate |
| $v$ | Poisson's ratio |
| v, $\bar{\mathbf{v}}$ | Fluid velocity and predefined fluid velocity tensors |
| $v_{12}, v_{34}$ | Transverse flow rates at surfaces 1–2 and 3–4 |
| $v_x, v_y$ | Longitudinal and transverse flow velocity |
| $w$ | Displacement of surface footing |
| $x', y'$ | Longitudinal and transverse directions of the interface |
| $\gamma$ | Relative sliding displacement |
| $\gamma_c$ | Critical sliding distance |
| $\gamma_w$ | Unit weight of water |
| $\kappa$ | Slopes of normal compression line |
| $\lambda$ | Slope of swelling-recompression line |
| $\sigma, \sigma'$ | Total and effective stress tensor |
| $\sigma_n, \sigma_n'$ | Total and effective contact pressure |
| $\sigma_t, \sigma_t'$ | Total and effective shear stress |
| $\sigma'_v$ | Initial vertical effective stress |
| $\varphi, \varphi_{int}$ | Friction angles for soil and interface |
| $\alpha$ | Numerical integration parameter |
| $\varepsilon_q, \varepsilon_q{}^e$ | Total and elastic deviatoric strains of soil |
| $\varepsilon_V, \varepsilon_V{}^e, \varepsilon_V{}^p$ | Total, elastic, and plastic volumetric strains of soil |
| $\theta$ | Angle between coordinate systems *xOy* and *x'Oy'* |
| $\xi, \eta$ | Local coordinates of element |

## ACKNOWLEDGEMENT

The authors appreciate the discussions, guidance and review provided by Professor Mark Randolph from the Centre for Offshore Foundation Systems at the University of Western Australia. This research was undertaken with support from the Australia Research Council Discovery Projects DP190103315 and DP180103314.

Open access publishing facilitated by The University of Melbourne, as part of the Wiley – The University of Melbourne agreement via the Council of Australian University Librarians.

## DATA AVAILABILITY STATEMENT

The data that support the findings of this study are available from the corresponding author upon reasonable request.

## ORCID

*Yinghui Tian* https://orcid.org/0000-0002-0874-2346

## REFERENCES

1. Goodman RE, Taylor RL, Brekke TL. A model for the mechanics of jointed rock. *J Soil Mech Found Div*. 1968;94(3):637-659.
2. Beer G. An isoparametric joint/interface element for finite element analysis. *Int J Numer Methods Eng*. 1985;21(4):585-600.
3. Gens A, Carol I, Alonso EE. A constitutive model for rock joints formulation and numerical implementation. *Comput Geotech*. 1990;9(1-2):3-20.
4. Day RA, Potts DM. Zero thickness interface elements—numerical stability and application. *Int J Numer Anal Methods Geomech*. 1994;18(10):689-708.
5. Desai CS, Zaman MM, Lightner JG, Siriwardane HJ. Thin-layer element for interfaces and joints. *Int J Numer Anal Methods Geomech*. 1984;8(1):19-43.
6. Sharma KG, Desai CS. Analysis and implementation of thin-layer element for interfaces and joints. *J Eng Mech*. 1992;118(12):2442-2462.
7. Das BM, Shin EC, Dass RN, Omar MT. Suction force below plate anchors in soft clay. *Mar Georesources Geotechnol*. 1994;12(1):71-81.
8. Rowe RK, Davis EH. The behaviour of anchor plates in clay. *Geotechnique*. 1982;32(1):9-23.
9. Acosta-Martinez HE, Gourvenec S, Randolph MF. Centrifuge study of capacity of a skirted foundation under eccentric transient and sustained uplift. *Géotechnique*. 2012;62(4):317-328.
10. Li X. *The uplift of offshore shallow foundations*. Perth: University of Western Australia; 2015.
11. Mana DS, Gourvenec S, Randolph MF. Numerical modelling of seepage beneath skirted foundations subjected to vertical uplift. *Comput Geotech*. 2014;55(1):150-157.
12. Ng KL, Small JC. Behavior of joints and interfaces subjected to water pressure. *Comput Geotech*. 1997;20(1):71-93.
13. Segura JM, Carol I. Coupled HM analysis using zero-thickness interface elements with double nodes—Part II: verification and application. *Int J Numer Anal Methods Geomech*. 2008;32(18):2103-2123.
14. Segura JM, Carol I. On zero-thickness interface elements for diffusion problems. *Int J Numer Anal Methods Geomech*. 2004;28(9):947-962.
15. Guiducci C, Collin F, Radu JP, Pellegrino A, Charlier R, Numerical modeling of hydro-mechanical fracture behavior. In 10th ISRM Congress. 2003; OnePetro.
16. Cerfontaine B, Dieudonné AC, Radu JP, Collin F, Charlier R. 3D zero-thickness coupled interface finite element: formulation and application. *Comput Geotech*. 2015;69:124-140.
17. Zienkiewicz OC, Taylor RL. *The finite element method for solid and structural mechanics*. Elsevier; 2005.
18. Gerke HH, Van Genuchten MT. A dual-porosity model for simulating the preferential movement of water and solutes in structured porous media. *Water Resour Res*. 1993;29(2):305-319.
19. Larson RE, Higdon JJ. Microscopic flow near the surface of two-dimensional porous media. Part 2. Transverse flow. *J Fluid Mech*. 1987;178:119-136.
20. Snow DT. *A parallel plate model of fractured permeable media*. University of California; 1965.
21. Whitherspoon PA, Wang JS, Iwai K, Gale JE. Validity of the cubic law for fluid flow in a deformable rock fracture. *Water Resour Res*. 1980;16(6):1016-1024.
22. Tsang YW, Tsang CF. Channel model of flow through fractured media. *Water Resour Res*. 1987;23(3):467-479.
23. Brown SR. Fluid flow through rock joints: the effect of surface roughness. *J Geophys Res Solid Earth*. 1987;92(B2):1337-1347.
24. Thompson ME, Brown SR. The effect of anisotropic surface roughness on flow and transport in fractures. *J Geophys Res Solid Earth*. 1991;96(B13):21923-21932.
25. Oron AP, Berkowitz B. Flow in rock fractures: the local cubic law assumption reexamined. *Water Resour Res*. 1998;34(11):2811-2825.
26. Small JC, Booker JR, Davis EH. Elasto-plastic consolidation of soil. *Int J Solids Struct*. 1976;12(6):431-448.
27. Schellekens JC, De Borst R. On the numerical integration of interface elements. *Int J Numer Methods Eng*. 1993;36(1):43-66.
28. Cerfontaine B, Collin F, Charlier R. Numerical modelling of transient cyclic vertical loading of suction caissons in sand. *Geotechnique*. 2016;66(2):121-136.

29. Hu J, Ke H, Lan JW, Chen YM, Meng M. A dual-porosity model for coupled leachate and gas flow to vertical wells in municipal solid waste landfills. *Géotechnique*. 2020;70(5):406-420.
30. Roscoe K, Burland JB. *On the generalized stress-strain behaviour of wet clay*. Cambridege: 1968.
31. Schofield A, Wroth P. *Critical state soil mechanics*. London: McGraw-Hill; 1968.
32. Biot MA. General theory of three-dimensional consolidation. *J Appl Phys*. 1941;12(2):155-164.
33. Stewart DP. *Lateral loading of piled bridge abutments due to embankment construction*. Perth: The University of Western Australia; 1992.
34. Wroth CP. The interpretation of in situ soil tests. *Geotechnique*. 1984;34(4):449-489.
35. Finnie IMS, Randolph MF, Punch-through and liquefaction induced failure of shallow foundations on calcareous sediments. Proceedings of the international conference on behaviour of offshore structures, Boston, USA, 1994;217-230.
36. Prandtl L. Hauptaufsätze: Über die Eindringungsfestigkeit (Härte) plastischer Baustoffe und die Festigkeit von Schneiden. *ZAMM-J Appl Math Mech*. 1921;1(1):15-20. (in German).
37. Davis EH, Booker JR, The effect of increasing strength with depth on the bearing capacity of clays. Golden Jubilee of the International Society for Soil Mechanics and Foundation Engineering: Commemorative Volume. 1985;185.
38. Lehane BM, Gaudin C, Richards DJ, Rattley MJ. Rate effects on the vertical uplift capacity of footings founded in clay. *Géotechnique*. 2008;58(1):13-21.
39. Chen R, Gaudin C, Cassidy MJ. Investigation of the vertical uplift capacity of deep water mudmats in clay. *Can Geotech J*. 2012;49(7):853-865.



**How to cite this article:** Peng M, Tian Y, Gaudin C, Zhang L, Sheng D. Application of a coupled hydro-mechanical interface model in simulating uplifting problems. *Int J Numer Anal Methods Geomech*. 2022;46:3256–3280. https://doi.org/10.1002/nag.3450


## APPENDIX 1

Figure 16 shows a fluid element under force balance. The viscous shear stress is determined as:

$$\tau_1 = -\mu\frac{dv_1}{dy'};\tau_2 = -\mu\frac{dv_2}{dy'} \tag{A1}$$

where μ is the viscosity of the fluid; $v_{1x}$ and $v_{2x}$ the longitudinal velocities at the same locations as $\tau_1$ and $\tau_2$, respectively.

The hydraulic force difference at the two ends of the fluid element should balance the viscous shear force in Equation (A1). Therefore:

$$\int_{-r}^{r} dpdy' = (\tau_1 + \tau_2)\,dx \tag{A2}$$

where $r$ is the half width of the water element investigated, as shown in Figure 16.

Combining the above equations yields:

$$-\mu\frac{d(v_1 + v_2)}{dy'} = 2r\frac{dp_g}{dx'} + \frac{4r^3}{3g_n^2}\left(\frac{dp_{12}}{dx'} + \frac{dp_{34}}{dx'} - 2\frac{dp_g}{dx'}\right) \tag{A3}$$

Using the no-slip boundary conditions $v_1 = 0$ at $r = -g_n/2$ and $v_2 = 0$ at $r = g_n/2$ and integrating Equation (A3) give the distribution of longitudinal velocity for NS flow:

$$v_1 + v_2 = \frac{g_n^2 - 4r^2}{48\mu g_n^2}\left[\left(\frac{dp_{12}}{dx'} + \frac{dp_{34}}{dx'}\right)\left(g_n^2 + 4r^2\right) + \frac{dp_g}{dx'}\left(10g_n^2 - 8r^2\right)\right] \tag{A4}$$

Further integrating Equation (A4), the longitudinal flux of NS flow can be calculated as:

$$q_x = \int_0^{\frac{g_n}{2}} (v_1 + v_2)dy' = \frac{g_n^3}{120\mu}\left(\frac{dp_{12}}{dx'} + \frac{dp_{34}}{dx'} + 8\frac{dp_g}{dx'}\right) \tag{A5}$$